

The SOPHIE search for northern extrasolar planets.

XVII. A compact planetary system in a near 3:2 mean motion resonance chain

N. C. Hara¹*, F. Bouchy¹, M. Stalport¹, I. Boisse², J. Rodrigues¹, J.-B. Delisle¹, A. Santerne², G. W. Henry³, L. Arnold⁸, N. Astudillo-Defru⁵, S. Borgniet⁴, X. Bonfils⁴, V. Bourrier¹, B. Brugger², B. Courcol², S. Dalal⁹, M. Deleuil², X. Delfosse⁴, O. Demangeon¹⁰, R. F. Díaz^{6,7}, X. Dumusque¹, T. Forveille⁴, G. Hébrard^{9,8}, M. Hobson², F. Kiefer⁹, T. Lopez², L. Mignon⁴, O. Mousis², C. Moutou^{2,13}, F. Pepe¹, J. Rey¹, N. C. Santos^{10,11}, D. Ségransan¹, S. Udry¹, and P. A. Wilson^{14,15,9}

¹ Observatoire Astronomique de l'Université de Genève, 51 Chemin des Maillettes, 1290 Versoix, Switzerland e-mail: nathan.hara@unige.ch

² Aix Marseille Univ, CNRS, CNES, LAM, Marseille, France

³ Center of Excellence in Information Systems, Tennessee State University, Nashville, TN 37209, USA

⁴ Univ. Grenoble Alpes, CNRS, IPAG, 38000 Grenoble, France

⁵ Departamento de Matemática y Física Aplicadas, Universidad Católica de la Santísima Concepción, Alonso de Rivera 2850, Concepción, Chile

⁶ Universidad de Buenos Aires, Facultad de Ciencias Exactas y Naturales, Buenos Aires, Argentina

⁷ CONICET - Universidad de Buenos Aires, Instituto de Astronomía y Física del Espacio (IAFE), Buenos Aires, Argentina

⁸ Observatoire de Haute-Provence, CNRS, Aix Marseille Université, Institut Pythéas UMS 3470, 04870 Saint-Michel-l'Observatoire, France

⁹ Institut d'Astrophysique de Paris, UMR7095 CNRS, Université Pierre & Marie Curie, 98bis boulevard Arago, 75014 Paris, France

¹⁰ Instituto de Astrofísica e Ciências do Espaço, Universidade do Porto, CAUP, Rua das Estrelas, 4150-762 Porto, Portugal

¹¹ Departamento de Física e Astronomia, Faculdade de Ciências, Universidade do Porto, Rua do Campo Alegre, 4169-007 Porto, Portugal

¹² ASD/IMCCE, CNRS-UMR8028, Observatoire de Paris, PSL, UPMC, 77 Avenue Denfert-Rochereau, 75014 Paris, France

¹³ Canada-France-Hawaii Telescope Corporation, 65-1238 Mamalahoa Hwy, Kamuela, HI 96743, USA

¹⁴ Department of Physics, University of Warwick, Coventry CV4 7AL, UK

¹⁵ Centre for Exoplanets and Habitability, University of Warwick, Coventry CV4 7AL, UK

Received September 15, 1996; accepted March 16, 1997

ABSTRACT

Aims. Since 2011, the SOPHIE spectrograph has been used to search for Neptunes and Super-Earths in the northern hemisphere. As part of this observation program, 290 radial velocity measurements of HD 158259 were obtained. We present the analysis of this dataset.

Methods. The radial velocity data, corrected from instrument systematics, are analysed with classical and ℓ_1 periodograms. The stellar activity is modelled by a correlated Gaussian noise, and its impact on the planets detection is measured by a new technique based on cross-validation. Ancillary spectroscopic indices as well as photometric measurements are analysed to discuss the planetary origin of the signals. The stability of the system is assessed with numerical simulations.

Results. We report the detection of four planets in a chain of near 3:2 mean motion resonances around HD 158259 at 3.4, 5.2, 7.9 and 12 days, with a possible fifth planet at 17.4 days, also near the 3:2 resonance. Additionally, two low frequency signals are found in the data, and are attributed to a magnetic cycle and instrument systematics. The four planets are found to be outside of the two and three body resonances.

Conclusions.

1. Introduction

Transit surveys have unveiled several multi-planetary systems where the planets are tightly spaced and close to low order mean motion resonances (MMRs). For instance, Kepler-80 (Xie 2013; Lissauer et al. 2014), Kepler-223 (Borucki et al. 2011; Mills et al. 2016) and TRAPPIST-1 Gillon et al. (2016) present respectively 5, 4 and 7 planets in such configurations. These systems could be the result of a formation scenario where the planets encounter dissipation in the gas disk, are locked in resonance then migrate inwards before potentially leaving the resonance (Terquem & Papaloizou 2007; MacDonald et al. 2016).

The planetary systems cited above are compact in the sense that any two subsequent planets have a period ratio below 2. Such near resonant, compact systems are detectable by radial velocity, as demonstrated by follow up observations of transits (Lopez et al. 2019). Detections of compact, resonant systems with radial velocity only are however rare (HD 40307 (Mayor et al. 2009) and HD 215152 (Delisle et al. 2018) with three planets respectively near 2:1 - 2:1 and 5:3 - 3:2 configurations).

In the present work, we analyse the 290 SOPHIE radial velocity measurements of HD 158259, as well as ancillary indicators and photometric measurements. The detected radial velocity signals, compatible with a chain of near resonant planets, have an amplitude in the 1 – 3 m/s range. To confirm their planetary

* NCCR CHEOPS fellow

Table 1. Known stellar parameters of HD 158259. Parallax, coordinates, proper motion and radius are taken from Gaia Collaboration (2018), spectral type from Cannon & Pickering (1993), and V magnitude from Høg et al. (2000). Mass is from Chandler et al. (2016)

Parameter	Value
Right ascension (J2000)	17h 25min 24.05s
Declination (J2000)	+52.7906°
Proper motion (mas/y)	-91.047 \pm 0.055, -49.639 \pm 0.059
Parallax	36.93 ± 0.029 mas
Spectral type	G0
V magnitude	6.46
Radius	$1.21^{+0.03}_{-0.08} R_{\odot}$
Mass	$1.08 \pm 0.1 M_{\odot}$
$v \sin i$	2.9 km/s
$\log R'_{hk}$	-4.8

origin, it is critical to consider whether they could be due to the star or to instrument systematics. To this end, we include in the analysis several data sets: the bisector span and $\log R'_{hk}$ derived from the spectra, as well as photometric data. The periodicity search is done with a ℓ_1 periodogram (Hara et al. 2017) including a correlated noise model, selected with cross-validation. The results are compared to those of a classical periodogram (Balucic 2008). The orbital stability of the resulting system is checked with numerical simulations.

The article is structured as follows. The data and its analysis are respectively presented in sections 2 and 3. The stability of the system and its dynamical features are presented in section 4, and we conclude in section 5.

2. Data

2.1. HD 158259

HD 158259 is a G0 type star in the northern hemisphere with a V magnitude of 6.4. The known stellar parameters are reported in table 2.1. The stellar rotation period is not known precisely, but can be estimated. The median $\log R'_{hk}$ from SOPHIE measurements is -4.8. With the empirical relationship of Mamajek & Hillenbrand (2008), this translates to an estimated rotation period of 18 days. Besides, the SOPHIE radial velocity data gives $v \sin i = 2.9 \pm 1$ km/s (see Boisse et al. 2010). Assuming $i = 90^\circ$ and taking the GAIA radius estimate of $1.21 R_{\odot}$, the $v \sin i$ estimation yields a rotation period of $\approx 20 \pm 7$ days.

2.2. SOPHIE radial velocities

SOPHIE is an echelle spectrograph mounted on the 193cm telescope of the Haute-Provence observatory (Bouchy et al. 2011). Several surveys are conducted with SOPHIE: a moderate precision survey (3.5 - 7 m/s), aiming at detecting Jupiter-mass companions (Hébrard et al. 2016), as well as a search of smaller planets around M-dwarfs (e.g. Hobson et al. 2018, 2019; Díaz et al. 2019).

Since 2011, SOPHIE has been used for a survey of bright solar-type stars, with the aim of detecting Neptunes and Super-Earths (Bouchy et al. 2011). For all the observations performed in this survey, the instrumental drift is measured and corrected for by recording on the detector, close to the stellar spectrum, the spectrum of a reference lamp. This one is a thorium-argon lamp before RJD 57032 and a Fabry-Perot interferometer after

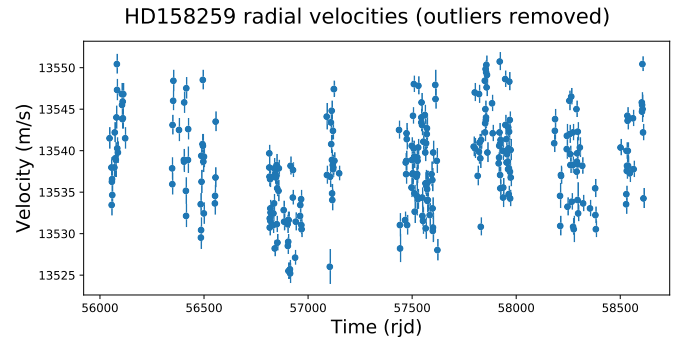


Fig. 1. SOPHIE radial velocity measurements of HD 158259 after outliers at bjd 2457941.5059, 2457944.4063, 2457945.4585 have been removed.

this date. The observations of HD 158259 were part of this program. 290 measurements were obtained, with an average error of 1.2 m/s. The data, corrected from outliers (see section 3.2.1), is shown in Fig. 1.

The radial velocity is not the only data product extracted from the SOPHIE spectra. The bisector span (Queloz et al. 2001) as well as the $\log R'_{hk}$ (Noyes 1984) are also extracted and leveraged in the analysis.

2.3. Photometry

The photometry has been obtained with the T11 telescope at the Automatic Photoelectric Telescopes (APTs), located at Fairborn Observatory in southern Arizona. The data, covering four observation seasons, is processed as described in Henry (1999). We consider the photometric flux relative to three comparison stars, where the data of each observational season is normalized by its mean value.

3. Analysis of the data sets

3.1. Photometry and ancillary indicators

If the bisector span, $\log R'_{hk}$ or photometry show signs of temporal correlation, in particular periodic signatures, this might mean that the RVs are corrupted by stellar or instrumental effects (e.g. Queloz et al. 2001).

To search for correlations and periodicities in the photometry and ancillary indicators, we compute their generalised Lomb-Scargle periodogram (Ferraz-Mello 1981; Zechmeister & Kürster 2009) on a grid of frequencies spanning from 0 to 1.5 cycles/day, and report the strongest periodic signatures. The false alarm probabilities (FAP) of the highest peaks of the periodograms are computed using the Balucic (2008) analytical formula. After computing the periodogram and checking that no significant high frequency signal is found, we perform the search on a grid of frequencies from 0 to 0.95 cycle/day to avoid aliases in the one day region. We subtract iteratively signals at the periods found and compute the periodograms of the residuals. We also apply ℓ_1 periodograms for comparison. The analysis is presented in detail in appendix A, we here report its main results.

The analysis of the $\log R'_{hk}$ periodogram supports the presence of a magnetic cycle with a period ≥ 1500 d. The bisector span presents several periods (552, 85 and 11.5 d with FAPs 0.13, 0.21 and 0.25) which might hint the presence of correlated noise in the radial velocity data. The photometry presents two potential periodicities, though with high false alarm probabilities (108 and 11.5 d with FAPs 0.75 and 0.43). The fact that the

signal at 11.5 days appears both in the bisector and photometry – in both case with low significance – might indicate weak stellar effects at this period. As we shall see, it is not present in the radial velocity data.

3.2. Radial velocities

3.2.1. Accounting for instrumental effects

SOPHIE experiences a drift of the zero velocity point due to several factors: change of fiber, calibration lamp ageing and other systematic effects. A drift estimate is obtained by observing reference stars, deemed to have a nearly constant velocity, each night of observations. The reference stars velocities are combined and interpolated to create an estimate of the drift as a function of time. This one is then subtracted to all the time series of the observation program. The estimation procedure, close to Courcol et al. (2015), is presented in detail in Hara et al. (2019a).

In the obtained time series, there might remain outliers, most likely due to bad observation conditions. To remove those, we compute the mean absolute deviation (MAD) of the data set and compute $\sigma = 1.48 \text{ MAD}$, which is the relation between the standard deviation σ and the MAD of a Gaussian distribution. We exclude the data points if their absolute difference to the median is greater than $k \times \text{MAD}$ with $k = 4$. This leads to removing three measurements at barycentric Julian day (bjd) 2457941.5059, 2457944.4063, 2457945.4585.

3.2.2. Period search

To search for potential periodicities in the radial velocities, we compute the ℓ_1 periodogram of the data, as defined in Hara et al. (2017). This tool is based on sparse recovery techniques, more specifically the basis pursuit algorithm (Chen et al. 1998). It takes in input a frequency grid on which periods are searched, and an assumed covariance matrix of the noise. The ℓ_1 periodogram outputs a figure which has a similar aspect to a regular periodogram, but with fewer peaks due to aliasing.

The detected signals might significantly vary from one noise model to another. To explore the sensitivity of the detection, we consider several noise models, which are ranked with a procedure based on cross-validation, as explained in appendix B. For the covariance matrix corresponding to the best cross validation score and a grid of equispaced frequencies between 0 and 0.7 cycle/day, the ℓ_1 periodogram of the SOPHIE radial velocities is represented in Fig. 3. Note that the y axis unit is in m/s, but the amplitudes cannot be interpreted as estimates of the semi amplitudes of the planets and are expected to be much smaller (Hara et al. 2017).

The peaks of the ℓ_1 -periodograms can be assigned a FAP, which is interpretable as the FAP of a regular periodogram peak. For the peaks pointed by red markers in Fig. 3, the FAPs are given in table 3.3. The FAP values suggest the presence of signals, in decreasing strengths of detection, at 3.43, 5.19, 7.95, 12.0, 2021, 362 and 17.4 days, while the signals at 1.84, 17.7 and 34.5 are found not to be significant. In appendix B, we explore the sensitivity of this result to the noise model. We find that the detection of signals at 3.43, 5.19, 7.95, 12.0, 1969, 365 and 17.4 days are robust, with a lower evidence for 17.4 days. We fit a model with sinusoidal functions initialised at the six significant periods. The data phase-folded at the fitted periods is shown in Fig. 2. In appendix C, the results are compared to a classical periodogram approach, which gives similar results.

A six planet fit yields residuals of rms 3.77 m/s, which is higher than the nominal uncertainties of the SOPHIE data (1.2 m/s). We studied the residuals with the methods of Hara et al. (2019b), and found correlations in the residuals, which might corrupt the orbital element estimates. In appendix D, we show that the six periodic signals found, a noise model including a white and correlated noise components yields a consistent model of the data. We now discuss the origin of the detected periodicities.

3.3. Periodicity origin

The ℓ_1 periodogram peaks at 2020 and 362 days are unlikely to indicate the presence of long period planets. Indeed, a period in the vicinity of 2020 days, with a strong statistical significance, appears in the $\log R'_{HK}$ periodogram, so that it most likely stems from a magnetic cycle. The 362 days signal is fully compatible with a yearly signal and is attributed to a systematic effect in the instrument.

The periods at 3.43, 5.19, 7.95 and 12.0 days are most likely planets (from now on denoted by HD 158259 b, c, d, e). Indeed, none of these periods appear clearly in the bisector span, $\log R'_{hk}$ or photometry. Secondly, if apparent 2:1 MMRs can in fact be eccentric planets, it is very unlikely to happen for planets in near 3:2 resonance (Hara et al. 2019b). Thirdly, the periods could be due to instrument systematics. We find it unlikely, since the periods do not consistently appear in the 123 other data sets of the survey HD 158259 is part of (Hara et al. 2019a).

Most importantly, the period ratio of two subsequent planets is very close to 3:2, namely 1.51, 1.53 and 1.51. Pairs of planets close to the 3:2 period ratio are known to be common (Lissauer et al. 2011; Steffen & Hwang 2015), and it seems unlikely that the stellar features would mimic this specific spacing of periods.

The origin of the periodicity at 17.4 days is more uncertain. Its statistical significance is lower than the other planets and most importantly, 17.4 is close to the rotation period estimated from the $\log R'_{HK}$ of 18 days (see section 2.1). However, its period ratio with the 12 days planet is 1.44, which is close to the 3:2 mean motion resonance, though further away than the other planets. It could happen that the planet is synchronised with the stellar rotation period, but the current data does not allow to conclude on that point. Indeed, setting a quasi-periodic term in the covariance model suppresses the 17.4 d periodogram peak. In conclusion, the presence of a planet at 17.4 days cannot be firmly confirmed.

3.4. Orbital elements

To derive the uncertainties on the orbital elements of the planets, we compute credible intervals with a Monte Carlo Markov chain algorithm (MCMC).

The model includes the 6 signals that seem significant from the analysis of section 3, as listed in the upper part of table 3.3. The 17.4 signal is included even though its detection is marginal. Indeed, not including this signal would mean that it would be partially absorbed in the fit of the other orbital elements, and lead to biased estimates and too narrow error bars. We also include a correlated noise model with an exponential decay. The dynamical analysis showed that eccentricities above 0.1 lead to unstable solutions for inclination = 90° (see section 4, the prior was chosen to strongly disfavour $e > 0.1$, and the posterior distribution does not allow to put constraints on e nor ω . The details of the analysis are presented in appendix D.

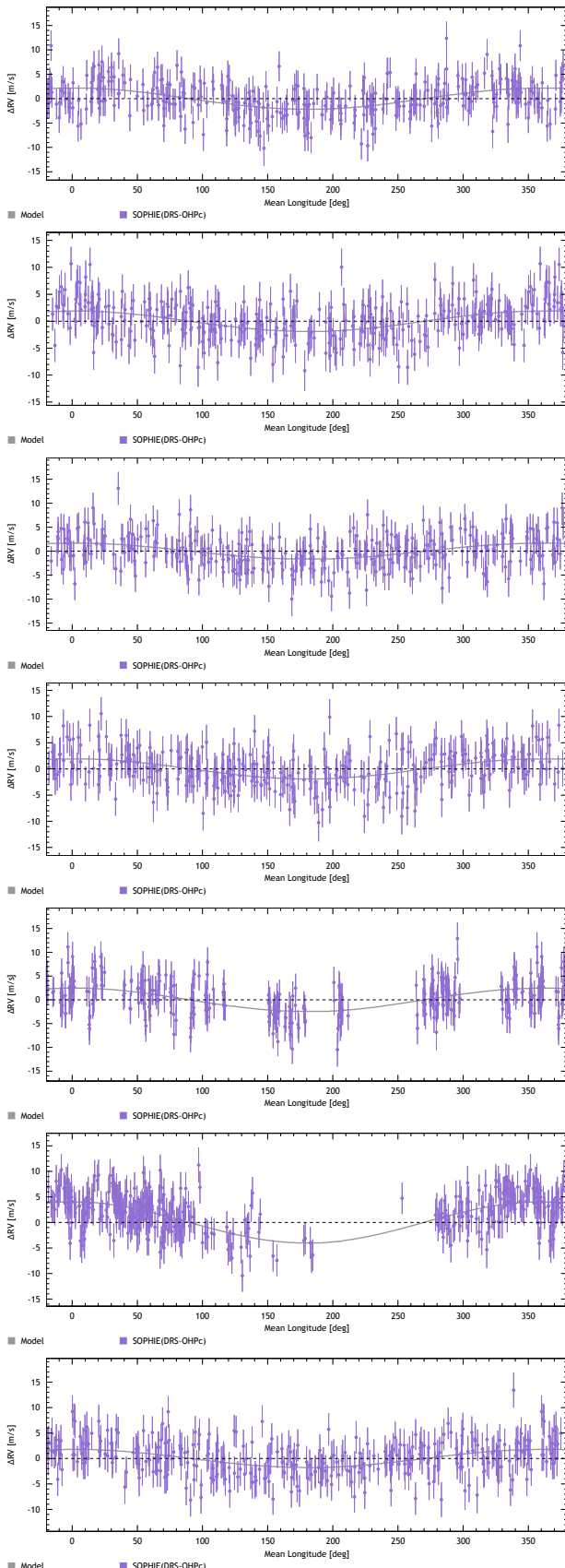


Fig. 2. Radial velocity phase-folded at the periods of the signals appearing in the period analysis. From top to bottom: 3.43, 5.19, 7.95, 12.0, 17.7, 362 and 17.4 d.

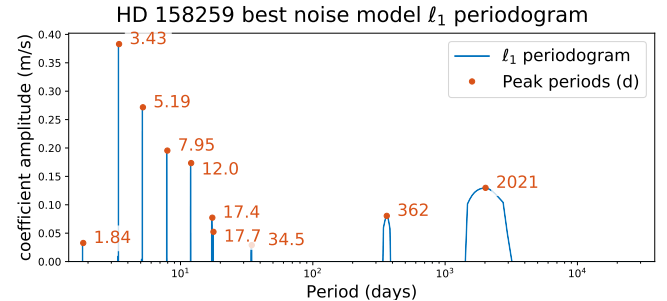


Fig. 3. ℓ_1 periodogram of the SOPHIE radial velocities of HD 158259 corrected from outliers (in blue). The periods at which the main peaks occur are represented in red.

Table 2. Periods appearing in the ℓ_1 periodogram and their false alarm probabilities with their origin, the semi-amplitude of corresponding signals and $M \sin i$ with 68.7% intervals

Peak period (d)	FAP	Origin	K (m/s)	$M \sin i$ (M_{\oplus})
3.432	1.6e-07	Planet <i>b</i>	$2.2_{-0.2}^{+0.2}$	$5.5_{-0.6}^{+0.6}$
5.198	5.9e-05	Planet <i>c</i>	$1.9_{-0.3}^{+0.2}$	$5.3_{-0.7}^{+0.7}$
7.954	1.7e-04	Planet <i>d</i>	$1.8_{-0.3}^{+0.3}$	$5.8_{-1.0}^{+0.9}$
12.03	6.1e-03	Planet <i>e</i>	$1.7_{-0.3}^{+0.3}$	$6.4_{-1.3}^{+1.3}$
2020	1.1e-03	Activity	$2.9_{-0.4}^{+0.4}$	
362	1.3e-02	Systematic	$3.4_{-0.8}^{+0.7}$	
17.39	1.3e-02	Candidate	$1.6_{-0.3}^{+0.4}$	$6.9_{-1.6}^{+1.6}$
Non significant signals				
1.77	0.74	-	-	-
1.839	0.54	-	-	-
34.5	1.0	-	-	-

The main features of the planets and fitted signals are reported in table 3.3. In summary, the system exhibits four planets with similar $m \sin i \approx 6M_{\oplus}$. Furthermore, there appears to be a signal at ≈ 2000 d and a yearly signal with amplitudes $K \approx 3$ m/s, most likely due to activity and instrumental effects respectively. Finally, there is a candidate planet which would also have $m \sin i \approx 6M_{\oplus}$. We find a significantly non zero correlation time-scale of the noise of $4.9_{-1.7}^{+1.2}$ d. We note that the similarity in mass of the planets is compatible with the hypothesis that planets within the same system have similar sizes (Weiss et al. 2018). In the next section, we present our dynamical study of the system.

4. Dynamical analysis

For the dynamical analysis of the system, we consider the planets *b*, *c*, *d*, *e* only, whose period ratios are close to the 3:2 MMRs. We compute a stability map in the vicinity of the circular model maximum likelihood fit. The system is supposed co-planar and edge-on ($i = 90$ deg), and ω is fixed to 0. The eccentricity and period of planet *c* are explored uniformly in given windows ($e_c \in [0.0, 0.15]$, $P_c \in [5.0, 5.4]$ days). The map is constituted of 22801 (151x151) sets of initial conditions. Each set was integrated 1 kyr in the future using the 15-th order N-body integrator IAS15 (Rein & Spiegel 2015), from

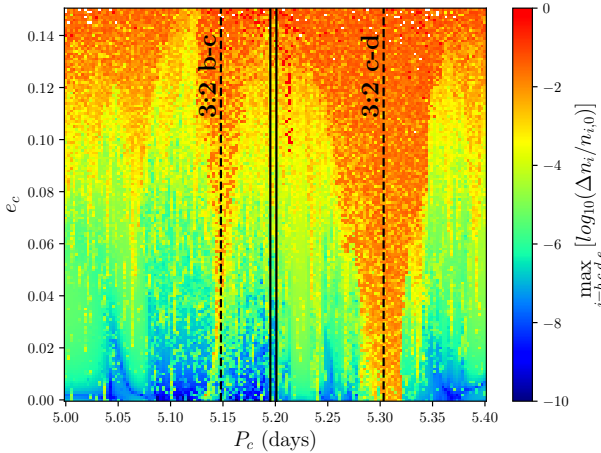


Fig. 4. Stability map of HD158259 c around the maximum likelihood solution of the circular model. In the color bar legend, Δn_i is the difference, for every planet, between the average mean motion over each half of the integration $T/2$, where $T = 1\text{kyr}$, and $n_{i,0}$ is the initial mean motion (where $i = b, c, d$ or e). The two vertical continuous lines represent the borders of the 3σ credible interval on the period. The dashed lines identify the exact locations of the 3:2 MMRs, between planets b and c and between planets c and d.

the package REBOUND¹ (Rein & Liu 2012). General relativity was included via REBOUNDx, using the model of Anderson et al. (1975). To compute the orbital stability, we used the NAFF chaos indicator (Laskar 1990, 1993). The resulting map is shown in Fig. 4, where blue and red correspond respectively to stable and unstable regions.

First, we observe the existence of stable solutions for the current estimation of the parameters at low eccentricities of planet c, and that values of e_c larger than ~ 0.1 are unlikely. Secondly, HD 158259 c lies in between the two 3:2 MMRs, with planets b and d. Note that our conclusions may change if all the initial orbital elements were simultaneously allowed to vary. Indeed, except e_c and P_c , all the initial parameters are fixed. However, the fact that HD 158259 c is neither in resonance with b nor d is robust as the period ratio is significantly outside these regions.

While the planets in the HD 158259 system clearly are outside of the 3:2 MMRs, they could still be locked in three planets resonances, with a libration of the so-called Laplace angles (e.g. Charalambous et al. 2018). Following Delisle (2017), we find that if it were the case, the Laplace angles, defined as

$$\begin{aligned}\phi_{123} &= 3\lambda_3 + 2\lambda_1 - 5\lambda_2 \approx \pi, \\ \phi_{234} &= 3\lambda_4 + 2\lambda_2 - 5\lambda_3 \approx \pi,\end{aligned}\quad (1)$$

where λ_i is the mean longitude of planet i , should both librate around π . Moreover, if these angles librate, their derivatives should average out to zero over the libration period (e.g. Mills et al. 2016)

$$\begin{aligned}\frac{1}{2\pi} \langle \dot{\phi}_{123} \rangle &= \frac{3}{P_3} + \frac{2}{P_1} - \frac{5}{P_2} \approx 0, \\ \frac{1}{2\pi} \langle \dot{\phi}_{234} \rangle &= \frac{3}{P_4} + \frac{2}{P_2} - \frac{5}{P_3} \approx 0,\end{aligned}\quad (2)$$

¹ The REBOUND code is freely available at <http://github.com/hannorein/rebound>.

where P_i is the orbital period of planet i . We looked at the distributions of ϕ_{123} , ϕ_{234} , as well as their derivatives in the posteriors of the MCMC and conclude that the system is not locked either in these Laplace resonances.

Nevertheless, period ratios so close to 3:2 cannot be explained by pure randomness. It is therefore probable that during the migration of the planets in the protoplanetary disk, they were locked in a 8:12:18:27 chain (with each consecutive pair of planet locked in 3:2 MMR). The currently observed departure from exact commensurability might be explained by tidal dissipation, as it was already proposed for similar Kepler systems (e.g. Delisle & Laskar 2014).

5. Conclusion

In this work, we have analysed 290 SOPHIE measurements of HD 158259. The analysis of the radial velocity data, including a correction of the instrument drift and over a thousand correlated noise models, supports the detection of four to five planets. The detection of planets at 3.43, 5.19, 7.95, 12.0 d is strongly supported by the data, and there exists stable configurations compatible with the error bars. A signal at 17.4 d could be due to a planet, but is marginally significant and close to the predicted rotation period. As a consequence, its planetary origin cannot be confirmed.

While many compact near-resonance chains have been detected by transits, they have so far been rare in radial velocity surveys. The present analysis shows that they can be detected, provided there enough data points, and an appropriate accounting of correlated noises (instrumental and stellar).

The four detected planets are such that subsequent planets have period ratios close to but slightly higher than 3:2, and the system is also found not to be in Laplace resonances. The potential fifth planet is close to, but slightly below a 3:2 period ratio with the planet e. This orbital configuration is very similar to what was found by the Kepler survey, where the distribution of period ratios in multiplanetary systems shows a peak around 1.52, i.e. slightly higher than 3:2 (see Lissauer et al. 2011; Fabrycky et al. 2014), and is consistent with existing formation scenarios (e.g. Terquem & Papaloizou 2007; Delisle & Laskar 2014; MacDonald et al. 2016).

Since the system is closely packed, the planetary perturbations are strong. Therefore, inclinations far from the value of 90 degrees are significantly disfavored, since they correspond to large planet masses. This increases the transit probability. HD 158259 has been observed by TESS (Ricker et al. 2014; Sullivan et al. 2015), whose upcoming results will confirm whether it transits or not. If it does, since the target is very bright (V magnitude of 6.4) it will be an excellent target for further characterization.

Acknowledgements. We warmly thank the OHP staff for their support on the observations. N.C.H. and J.-B. D. acknowledge the financial support of the National Centre for Competence in Research PlanetS of the Swiss National Science Foundation (SNSF). This work was supported by the Programme National de Planétologie (PNP) of CNRS/INSU, co-funded by CNE. G.W.H. acknowledges long-term support from NASA, NSF, Tennessee State University, and the State of Tennessee through its Centers of Excellence program. X.De., X.B., I.B., and T.F. received funding from the French Programme National de Physique Stellaire (PNPS) and the Programme National de Planétologie (PNP) of CNRS (INSU). X.B. acknowledges funding from the European Research Council under the ERC Grant Agreement n. 337591-ExTrA. This work has been supported by a grant from Labex OSUG@2020 (Investissements d’avenir – ANR10 LABX56). This work is also supported by the French National Research Agency in the framework of the Investissements d’Avenir program (ANR-15-IDEX-02), through the funding of the ‘Origin of Life’ project of the Univ. Grenoble-Alpes. V.B. acknowledges support from the Swiss National Science

Foundation (SNSF) in the frame of the National Centre for Competence in Research PlanetS, and has received funding from the European Research Council (ERC) under the European Unions Horizon 2020 research and innovation programme (project Four Aces; grant agreement No 724427). This work was supported by FCT - Fundação para a Ciência e a Tecnologia through national funds and by FEDER through COMPETE2020 - Programa Operacional Competitividade e Internacionalização by grants UID/FIS/04434/2013 & POCI-01-0145-FEDER-007672; PTDC/FIS-AST/28953/2017 & POCI-01-0145-FEDER-028953; and PTDC/FIS-AST/32113/2017 & POCI-01-0145-FEDER-032113. N.A-D. acknowledges support from FONDECYT #3180063. X.Du. is grateful to the Branco Weiss Fellowship—Society for continuous support.

References

Anderson, J. D., Esposito, P. B., Martin, W., Thornton, C. L., & Muhleman, D. O. 1975, *ApJ*, 200, 221

Baluev, R. V. 2008, *MNRAS*, 385, 1279

Boisse, I., Eggenberger, A., Santos, N. C., et al. 2010, *A&A*, 523, A88

Borucki, W. J., Koch, D. G., Basri, G., et al. 2011, *The Astrophysical Journal*, 736, 19

Bouchy, F., Hébrard, G., Delfosse, X., et al. 2011, in EPSC-DPS Joint Meeting 2011, Vol. 2011, 240

Cannon, A. J. & Pickering, E. C. 1993, *VizieR Online Data Catalog*, III/135A

Chandler, C. O., McDonald, I., & Kane, S. R. 2016, *VizieR Online Data Catalog*, J/AJ/151/59

Charalambous, C., Martí, J. G., Beaugé, C., & Ramos, X. S. 2018, *MNRAS*, 477, 1414

Chen, S. S., Donoho, D. L., & Saunders, M. A. 1998, *SIAM JOURNAL ON SCIENTIFIC COMPUTING*, 20, 33

Courcol, B., Bouchy, F., Pepe, F., et al. 2015, *A&A*, 581, A38

Delisle, J.-B. 2017, *A&A*, 605, A96

Delisle, J. B., Hara, N. C., & Ségransan, D. 2019, *a&A*, submitted

Delisle, J.-B. & Laskar, J. 2014, *A&A*, 570, L7

Delisle, J.-B., Ségransan, D., Dumusque, X., et al. 2018, *A&A*, 614, A133

Díaz, R. F., Delfosse, X., Hobson, M. J., et al. 2019, *A&A*, 625, A17

Fabrycky, D. C., Lissauer, J. J., Ragozzine, D., et al. 2014, *ApJ*, 790, 146

Ferraz-Mello, S. 1981, *AJ*, 86, 619

Foreman-Mackey, D., Agol, E., Ambikasaran, S., & Angus, R. 2017, *AJ*, 154, 220

Gaia Collaboration. 2018, *VizieR Online Data Catalog*, I/345

Gillon, M., Jehin, E., Lederer, S. M., et al. 2016, *Nature*, 533, 221

Hara, N. C., Bouchy, F., Boisse, I., et al. 2019a, in prep.

Hara, N. C., Boué, G., Laskar, J., & Correia, A. C. M. 2017, *MNRAS*, 464, 1220

Hara, N. C., Boué, G., Laskar, J., Delisle, J. B., & Unger, N. 2019b, *MNRAS*, 489, 738

Haywood, R. D., Collier Cameron, A., Queloz, D., et al. 2014, *MNRAS*, 443, 2517

Hébrard, G., Arnold, L., Forveille, T., et al. 2016, *A&A*, 588, A145

Henry, G. W. 1999, *PASP*, 111, 845

Hobson, M. J., Delfosse, X., Astudillo-Defru, N., et al. 2019, *A&A*, 625, A18

Hobson, M. J., Díaz, R. F., Delfosse, X., et al. 2018, *A&A*, 618, A103

Høg, E., Fabricius, C., Makarov, V. V., et al. 2000, *A&A*, 355, L27

Jones, D. E., Stenning, D. C., Ford, E. B., et al. 2017, *ArXiv e-prints* [[arXiv:1711.01318](https://arxiv.org/abs/1711.01318)]

Laskar, J. 1990, *Icarus*, 88, 266

Laskar, J. 1993, *Celestial Mechanics and Dynamical Astronomy*, 56, 191

Lissauer, J. J., Marcy, G. W., Bryson, S. T., et al. 2014, *ApJ*, 784, 44

Lissauer, J. J., Ragozzine, D., Fabrycky, D. C., et al. 2011, *ApJS*, 197, 8

Lopez, T. A., Barros, S. C. C., Santerne, A., et al. 2019, *arXiv e-prints* [[arXiv:1909.13527](https://arxiv.org/abs/1909.13527)]

MacDonald, M. G., Ragozzine, D., Fabrycky, D. C., et al. 2016, *AJ*, 152, 105

Mamajek, E. E. & Hillenbrand, L. A. 2008, *ApJ*, 687, 1264

Mayor, M., Udry, S., Lovis, C., et al. 2009, *A&A*, 493, 639

Mills, S. M., Fabrycky, D. C., Migaszewski, C., et al. 2016, *Nature*, 533, 509

Noyes, R. W. 1984, in *Space Research in Stellar Activity and Variability*, ed. A. Mangeney & F. Praderie, 113

Queloz, D., Henry, G. W., Sivan, J. P., et al. 2001, *A&A*, 379, 279

Rasmussen, C. E. & Williams, C. K. I. 2005, *Gaussian Processes for Machine Learning (Adaptive Computation and Machine Learning)* (The MIT Press)

Rein, H. & Liu, S. F. 2012, *A&A*, 537, A128

Rein, H. & Spiegel, D. S. 2015, *MNRAS*, 446, 1424

Ricker, G. R., Winn, J. N., Vanderspek, R., et al. 2014, *Journal of Astronomical Telescopes, Instruments, and Systems*, 1, 1

Steffen, J. H. & Hwang, J. A. 2015, *MNRAS*, 448, 1956

Sullivan, P. W., Winn, J. N., Berta-Thompson, Z. K., et al. 2015, *The Astrophysical Journal*, 809, 77

Terquem, C. & Papaloizou, J. C. B. 2007, *ApJ*, 654, 1110

Tibshirani, R. 1994, *Journal of the Royal Statistical Society, Series B*, 58, 267

Weiss, L. M., Marcy, G. W., Petigura, E. A., et al. 2018, *AJ*, 155, 48

Xie, J.-W. 2013, *ApJS*, 208, 22

Zechmeister, M. & Kürster, M. 2009, *A&A*, 496, 577

Appendix A: Complementary analysis of the time series

In this section, we present complementary information for the analysis of the time series.

In Fig. A.1, we represent the periodogram of the photometric data. The maximum peak occurs at a period of 0.979 days, which is an alias of 11.6 days, and has a FAP of 0.33. The iterative search yields 11.63 and 108 days as dominant periods with FAPs of 0.75 and 0.43. Given the faintness of the two signals, they do not strongly point to intrinsically periodic phenomena on the surface of the star, or even correlations in the photometry.

The bisector span periodogram is presented in Fig. A.2. It presents peaks, in order of decreasing amplitude at 0.9857, 552, 85, 1576 and 23.5 days, where 0.9857 is an alias of 85 days. The false alarm probability of the highest peak is 0.08, which indicates that there is moderate evidence against the hypothesis that the bisector behaves like white noise. The iterative period search from 0 to 0.95 cycle/day points to signals at 550, 85 and 11.5 days with FAPs of 0.13, 0.21 and 0.25.

The $\log R'_{HK}$ periodogram (see Fig. A.3) presents a clear long term trend and, besides peaks in the one day region, peaks at 119 and 64 d. The iterative period search on a frequency grid from 0 to 0.95 cycle/day gives signals at 3500, 119 and 32 d, with FAPs $4 \cdot 10^{-12}$, 0.18 and 0.14. This analysis does not include all the $\log R'_{HK}$ measurements. The selection of the measurements is presented below.

In conclusion, the analysis of the photometry and ancillary indicators supports the existence of a long term magnetic cycle, appearing in the $\log R'_{HK}$ periodogram, with a period ≥ 1500 d. We note that the presence of several marginally significant periods in the bisector span might indicate the presence of correlated noise in the data. The fact that 11.5 days appears both in the bisector and photometry might indicate that there is a weak stellar feature at this period.

The analysis of the bisector span uses all the available data points, which is not the case for the $\log R'_{HK}$. The $\log R'_{HK}$ analysis is made on the values of the $\log R'_{HK}$ measured before jdb 58000. After this date, the values of the $\log R'_{HK}$ are not reliable due to technical difficulties, stemming from the change of the calibration system. We remove outliers from the time series with a criterion based on the median absolute deviation (MAD). We compute $\sigma = 1.48$ MAD, which is the relation between the standard deviation σ and the MAD of a Gaussian distribution. We exclude the data points if their absolute difference to the median is greater than $k \times \sigma$ with $k = 3.5$. The points selected for the analysis are presented in Fig. A.5 in blue, while the points excluded are represented in red.

Similarly, a criterion at 4σ applied to the RV time series leads to the removal of three outliers. In Fig. A.4, we show in green the three points removed from the analysis.

We now present the ℓ_1 periodograms of the bisector span and the $\log R'_{HK}$ (respectively Fig. A.7 and Fig. A.6), computed on a frequency grid from 0 to 0.95 cycles/day, to avoid the one day region. The highest peaks in the ℓ_1 periodogram of the bisector span occur at the same periodicities as the the peaks of the periodogram : 85, 556, 1505 and 23.5 d for the bisector and 2137, 119 and 64.2 d for the $\log R'_{HK}$. Furthermore, peaks at 1.77 d and 11.5 d are present in the ℓ_1 periodogram of the bisector span. The 11.5 periodicity might have a physical origin, as it also appears in the photometric data, however the significance levels of the periodicity are low and marginal in both data sets. None of the peaks of the bisector span ℓ_1 periodogram are very significant. Indeed, the significances of the peaks at 85, 11.5, 556, 1505, 1.77 and

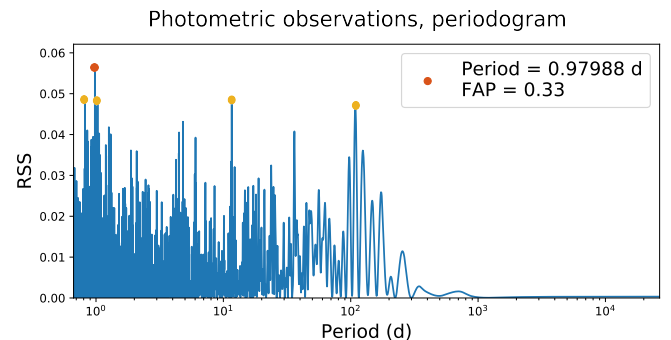


Fig. A.1. Periodogram of the photometric data computed between 0 and 1.5 cycle/d. The maximum peak is attained at 0.979 d (in red). The four subsequent tallest peaks are, in decreasing order, at 0.817 11.636, 1.028 and 108 d (in yellow).

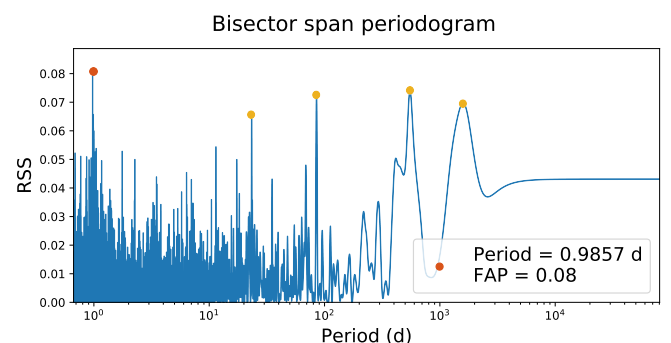


Fig. A.2. Periodogram of the bisector span computed on an equispaced frequency grid between 0 and 1.5 cycle/d. The maximum peak is attained at 0.985 d (in red). The four subsequent tallest peaks are, in decreasing order, at 552, 85.5, 1576 and 23.48 d (in yellow).

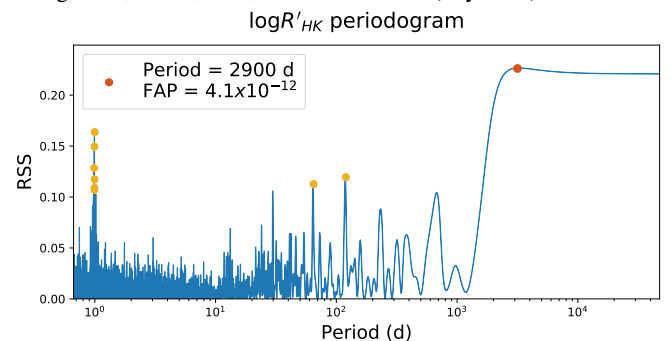


Fig. A.3. Periodogram of the $\log R'_{HK}$ computed on an equispaced frequency grid between 0 and 1.5 cycle/d. The maximum peak is attained at 2900 d (in red). Besides aliases in the one day region, there is a peak at 119 and 64 days.

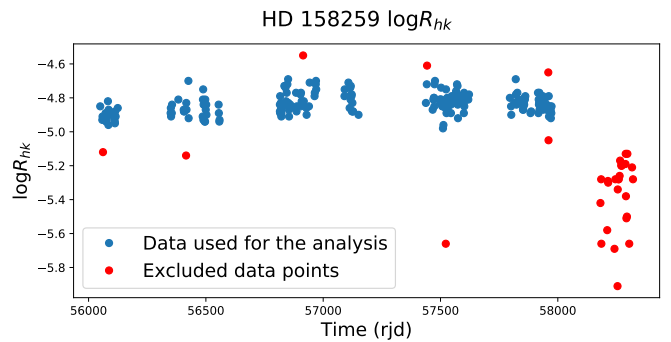


Fig. A.4. SOPHIE radial velocities and nominal 1σ error bars, the three points removed are shown in green.

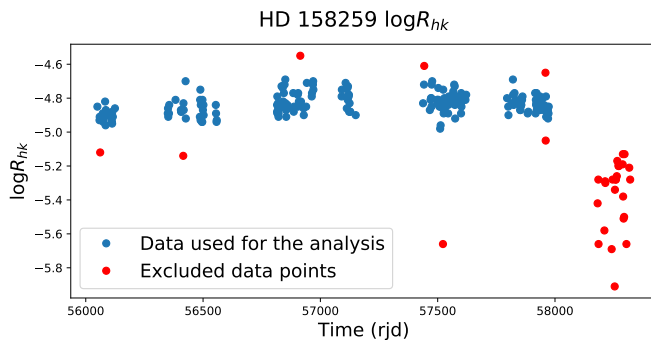


Fig. A.5. $\log R'_{HK}$ measurements of HD 158259. Points in blue are considered for the analysis, the points in red are excluded from the analysis.

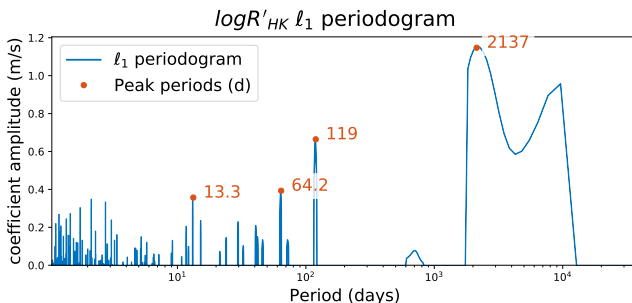


Fig. A.6. ℓ_1 Periodogram of the $\log R'_{HK}$.

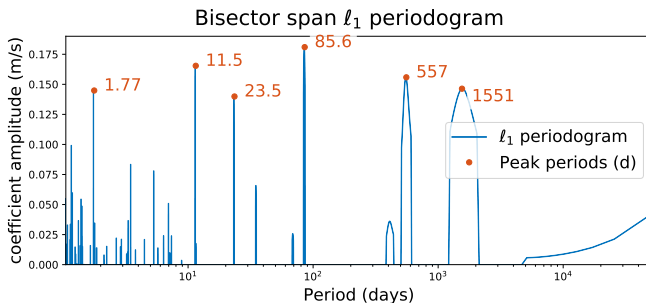


Fig. A.7. ℓ_1 Periodogram of the bisector span.

23.5 are 0.17, 0.557, 0.11, 1.0, 0.44 and 0.97. On the other hand, the 2137, 119 d periodicities in the $\log R'_{HK}$ present respectively a strong and moderate false alarm of 1.9×10^{-7} and 0.014. Note that the $\log R'_{HK}$ and bisector span are not expected to be sparse in the frequency domain, in the sense that they should be represented by a sum of a small number of sinusoidal components. On the contrary, planets should appear as pure sinusoidal signals, and one can search for a sparse representation of the RV signal. This explains why the ℓ_1 periodogram of the radial velocity is presented in the body of the text, while the it is presented in the appendices for the bisector and $\log R'_{HK}$.

Appendix B: Impact of the noise model on the detection

Appendix B.1: Selection with cross validation

Fig. 3 is obtained with a correlated noise model. In this section, we present the noise model chosen and the sensitivity of the detection to the noise model.

The various sources of noise in the RV are modelled as in Haywood et al. (2014) by a correlated Gaussian noise model.

In practice, one chooses a parametrization of the covariance matrix of the noise $V(\theta)$, where the element of V at index k, l depends on $|t_k - t_l|$ and a vector of parameters θ . In the following analysis, the parametrization chosen for V is such that its element at index k, l is

$$V_{kl}(\theta) = \delta_{k,l}(\sigma_k^2 + \sigma_W^2) + \sigma_C^2 c(k, l) + \sigma_R^2 e^{-\frac{|t_k - t_l|}{\tau_R}} + \sigma_{QP}^2 e^{-\frac{|t_k - t_l|}{\tau_{QP}}} \frac{1}{2} \left(1 + \cos\left(\frac{2\pi(t_k - t_l)}{P_{act}}\right)\right) \quad (\text{B.1})$$

Where σ_k is the nominal measurement uncertainty, σ_W is an additional white noise, σ_C is a calibration noise, where c equals one if measurements k and l are taken within the same night and to zero otherwise. σ_R and τ_R parametrize a correlated noise, which might originate from the star or the instrument. σ_{QP} , τ_{QP} and P_{act} parametrize a quasi-periodic covariance, which would originate from spots or faculae. The form of this covariance is compatible with the `spleaf` software (Delisle et al. 2019) and, except for the calibration noise, the CELERITE model (Foreman-Mackey et al. 2017).

To study the sensitivity of the detection to the noise model $\theta = (\sigma_W, \sigma_C, \sigma_R, \tau_R, \sigma_{QP}, \tau_{QP}, P_{act})$, we proceed by cross validation. We here give a brief outline of the procedure which is described in detail in Hara et al. (2019a). We first consider a grid of possible values for each component of θ . For instance, $\sigma_W = 0, 1, 2 \text{ m/s}$, $\sigma_C = 0, 1, 2$ etc. The θ with all the possible combinations of the values of its components are generated, and the corresponding covariance matrices are created according to eq. (B.1). If it is positive definite, it is added to the list of candidate covariance matrix.

The particular values taken in the present analysis are reported in table B.2. By default, we add a 2 m/s white noise and 0.75 cm/s calibration noise. The decay time scales of the red (R) and quasi periodic components include 0, in which case they are white noise jitters. The σ_R and σ_{QP} are chosen such that, when $\tau_R = \tau_{QP} = 0$ there exists a value of $\sigma_W^2 + \sigma_C^2 + \sigma_R^2 + \sigma_{QP}^2$ that is greater than the total variance of the data, and we subdivide the possible values of σ_R, σ_{QP} in smaller steps. The correlation timescales of $\tau_R = 0, 1$ and 6 correspond to no correlation, noise correlated on subsequent times of observations, or on a whole run of observation, which is typically 6 days. The P_{rot} candidate corresponds to peaks that appear in the period analysis of the radial velocity (17.4, 34.5 d) or in the bisector span (85 d).

For each matrix in the list of candidate noise model, the ℓ_1 periodogram is computed, and the frequencies that have a peak with $\text{FAP} < 0.05$ are selected. We select 70% of the data points randomly – the training set – and fit a sinusoidal model at the selected frequencies on this point. On the remaining 30% – the test set, we compute the likelihood of the data knowing the model fitted. The operation of selecting of a training set randomly and evaluating the likelihood on the test set is repeated 200 times. We take the median of the 200 values of the likelihood as the cross validation score of the noise model. As a result of this procedure, each noise model has a cross validation score (CV score).

In Fig. B.1, we represent the histogram of the values of the CV score for all the noise models considered. The model with the 20% highest CV score are represented in blue, and present similar values of the CV score. We call the set of these models CV_{20} .

Each model of CV_{20} might lead to different peaks selected with the $\text{FAP} < 0.05$ criterion. The periods and FAPs of the peaks selected are represented in Fig. B.2 by the yellow points. For the comparison with the best models, that is the model with maximum CV score, the periods appearing in the best model (red dots

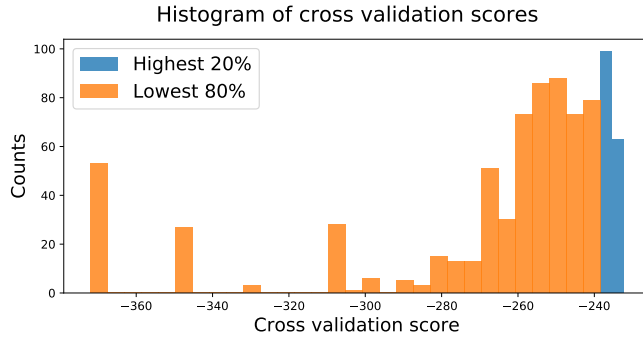


Fig. B.1. Histogram of the values of the cross validation score. Best 20% and lowest 80% are represented respectively in blue and orange.

in Fig. 3) are represented by the blue dashed lines. The signals at 3.43, 5.19, 7.95, 12.0, 17.4, 362 and 2020 days all appear in all of the CV_{20} models, except the 17.4 days which appears in only 86% of them. We represent the median of the FAPs for each of these periods in the CV_{20} and their FAP in the best models are represented in red for comparison. Note that the signals at 1.83 and 34.5 d are not included in the signals with $FAP < 0.05$ for the CV_{20} models, except once for 34.5 d. Finally, we note that a signal at ≈ 640 d is included in 9% of the CV_{20} models.

When using a LASSO-type estimator (Tibshirani 1994) such as the ℓ_1 periodogram, for a fixed dictionary (here, a fixed noise model), it is common practice to select the model with cross-validation as the solution follows the so-called LASSO path. This would here constitute a viable alternative to selecting the peaks that have $FAP < 0.05$. This was tested on a grid of parameters such as B.2, and yields very similar conclusions.

Appendix B.2: Long term model

It has been found that the $\log R'_{hk}$ has a strong long term signal. This one can be included in the analysis with a Gaussian process analysis, similarly to Haywood et al. (2014). We consider a simple covariance model for the $\log R'_{HK}$

$$V_{kl}(\theta) = \delta_{k,l} \sigma_W^2 + \sigma_C^2 c(k, l) + \sigma_R^2 e^{-\frac{(t_k - t_l)^2}{2\tau^2}} \quad (\text{B.2})$$

We assume that σ_R is equal to the standard deviation of the $\log R'_{HK}$ data, and fit the parameters σ_W and τ . We find $\sigma_W = 0.9\sigma_R$ and $\tau = 770$ d. We then predict the gaussian process value and its covariance with formulae 2.23, 2.24 in Rasmussen & Williams (2005). In Fig. B.4, we represent the raw $\log R'_{HK}$ data on which the fitting is made. The Gaussian process and the one sigma standard deviation of the marginal distribution at t are represented in light blue, and the prediction at the radial velocity measurement times in orange.

We then perform the same analysis as in section B.1, except that we include the smoothed $\log R'_{HK}$ (orange points in Fig. B.4) as a linear predictor in the model. The results are presented in Fig. B.3. These are almost identical to the results of section B.1, except that, as expected, the 2000 d signal disappears. We point out that the cross validation score of the best model is -236, while the best cross validation scores including a fitted long term sinusoid is -228, pointing to a very slight advantage for the sinusoidal model of the long trend, but they cannot be distinguished with certainty.

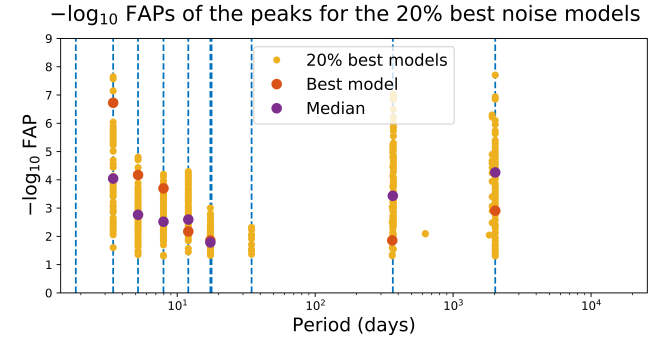


Fig. B.2. FAPs of the peaks of the 20% best models that have a FAP > 0.05 . The periods marked in red in Fig. 3 are represented by the blue dashed lines.

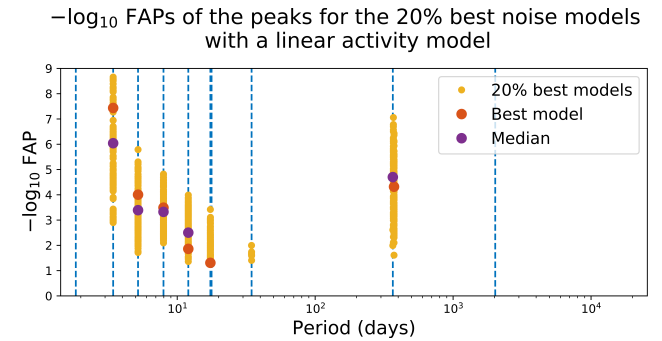


Fig. B.3. FAPs of the peaks of the 20% best models that have a FAP > 0.05 , when adding a linear activity model fitted as a Gaussian process. The periods marked in red in Fig. 3 are represented by the blue dashed lines.

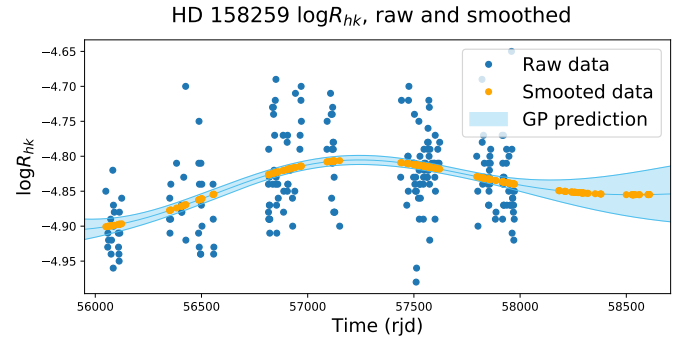


Fig. B.4. Raw and smoothed $\log R'_{HK}$. The dark blue points represent the raw $\log R'_{HK}$ data used for the prediction. The light blue lines represent the Gaussian process prediction and its $\pm 1\sigma$ error bars (see eq; (B.2)). The orange points are the predicted values of the Gaussian process at the radial velocity measurement times.

Appendix B.3: Discussion

We have found that signals at 3.43, 5.19, 7.95, 12.0, 17.4, 362 d consistently appear in the models with best cross validation score. The 2020 d signals appearing in section B.1 disappears when modelling the activity as in section B.2, pointing to a stellar origin. Overall, we claim that the 3.43, 5.19, 7.95, 12.0, 17.4, 362 d periodicities are present in the signal, with a lower confidence in the 17.4 period. Note that the analysis of section B.1 has also been made in a case where 23 d is replaced by 11.6 d in the array of noise models considered B.2, and the conclusions are identical.

Table B.1. Periods appearing in the ℓ_1 periodogram of the model with the highest CV score and their false alarm probabilities. The third columns show the percentage of models in the 20% best CV score (CV_{20} noise models) where the periodicity has a FAP<0.05, and the fourth column shows the median FAP of these periodocities in the CV_{20} models.

Peak period (d)	FAP	Inclusion in the model	median CV_{20} FAP
3.432	1.6e-07	100%	9e-05
5.198	5.9e-05	100%	1.7e-03
7.954	1.7e-04	100%	3e-03
12.03	6.1e-03	100%	2.5e-03
2020	1.1e-03	98%	5.4e-05
362	1.3e-02	98%	3.6e-04
17.39	1.3e-02	73%	1.6e-02
1.77	0.74	0.6%	-
1.839	0.54	0%	-
34.5	1.0	4%	-

Table B.2. Value of the parameters used to defined the grid of models tested.

Parameter	Values	Highest CV score
σ_w	2 m/s	2 m/s
σ_c	0.75 m/s	0.75 m/s
σ_r	0.1,2,3,4 m/s	3 m/s
τ_r	0,1,6 d	6 d
σ_{QP}	0,1,2 m/s	1 m/s
τ_{QP}	0, 20, 50, 100, 200	0 d
P_{act}	17.4, 23.5, 34.5, 85, 119 d	-

As a remark, the noise model selection procedure is close to Jones et al. (2017), except that comparing noise models with free parameters with cross validation, BIC and AIC, we compare models that are couples of noise model with fixed parameters and planets with fixed periods.

Appendix C: Periodogram analysis

In this section, we perform the period search in an iterative way. The procedure is as follows. We first compute at which frequencies the two maximum peak of the spectral windows are attained (besides the peak in $\omega = 0$ and denote them by ω_{S_1} and ω_{S_2} . Here, $\omega_{S_1} = 1.0027$ and $\omega_{S_2} = 0.999$ cycles/day.

The planet count is initialised at 0. We compute the generalised Lomb-Scargle periodogram, and search at which frequency its maximum is attained ω_0 . We then fit a Keplerian signal initialised at ω_0 , but depending on the value of ω_0 , we might choose to fit $\omega_0 - \omega_{S_i}$ instead, where $i = 1, 2$. We then add one to the planet count and compute the periodogram of the residuals, search the frequency corresponding to the maximum, ω_1 the maximum peak, then fit two Keplerian functions initialised at ω_0 and ω_1 , and so on until a non significant signal is found.

In Fig. C.1 we represent the subsequent periodograms, on a period range spanning from 0 to 1.5 cycles/day; computed iteratively. The periods selected at each iterations are marked in red, and their the false alarm probability corresponding to their peaks is given. It might happen that the maximum of the periodogram occurs at a period near 1 day, in which case the corresponding period is highlighted by a yellow vertical line. Since in each occurrence of this situations, there are peaks at longer period which are aliases of these ones, the peaks at longer periods are preferred.

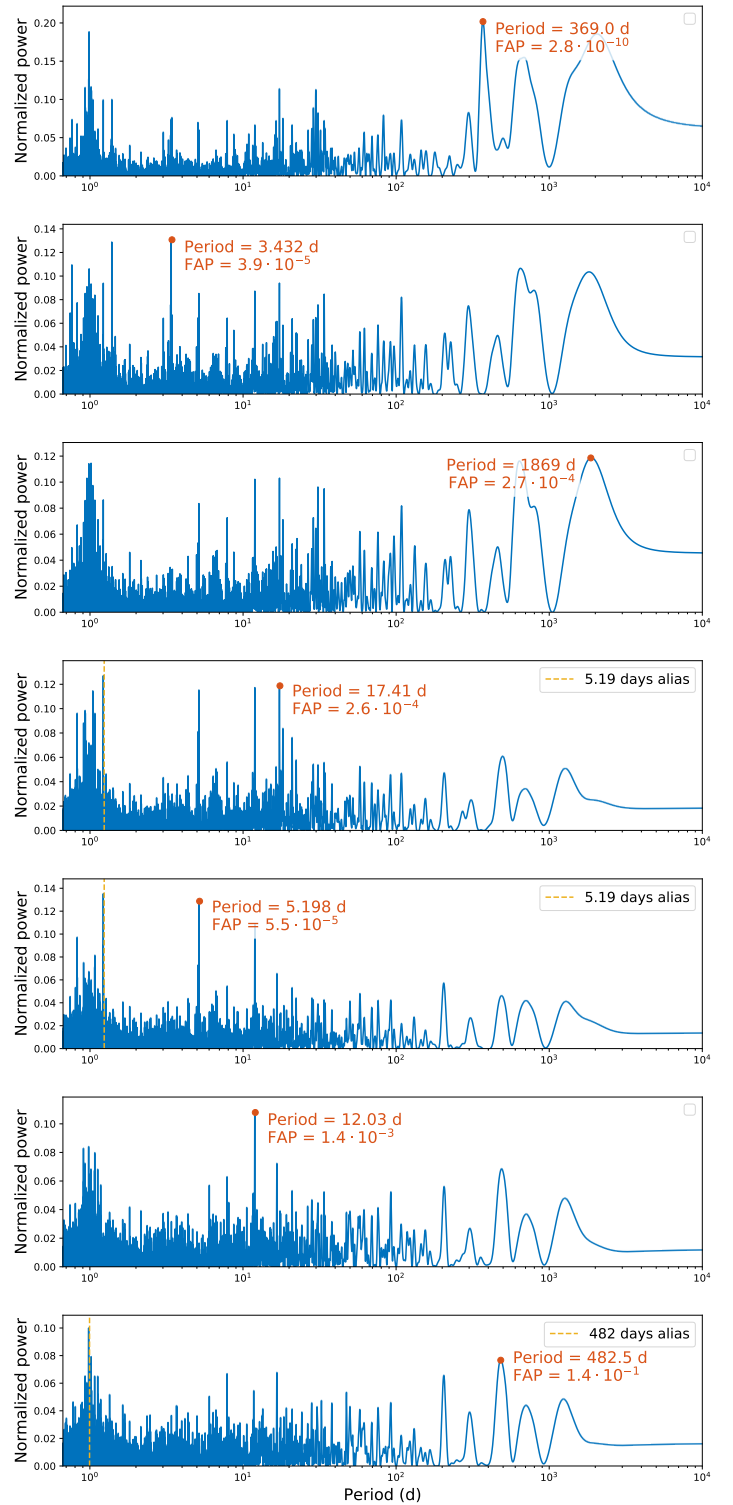


Fig. C.1. Subsequent periodograms after a fit of a Keplerian orbit model initialized at the maximum peak of the periodogram

Overall, we find the same results as the ℓ_1 periodogram, except that after the removal of the signals that are robust to noise models, there remains a significant peak at 0.99 days.

Table D.1. Variables used for the computation of the MCMC analysis and their prior distributions.

Parameter	prior
offset 1	Uniform on [-200, 200] km.s ⁻¹
smoothed rhk	Gaussian with mean 0 and $\sigma = 4$ m.s ⁻¹
P	Uniform (no specified bounds)
K	Uniform (no specified bounds)
λ_0 at bjd 2457500	Uniform on [0, 2π]
$\sqrt{e} \cos \omega$, $\sqrt{e} \sin \omega$	beta prior on e with $\alpha = 1$ and $\beta = 20$, uniform prior on ω on [0, 2π]
σ_w^2	Truncated Gaussian with $\sigma = 4$ m ⁻² .s ⁻²
σ_R^2	Truncated Gaussian with $\sigma = 4$ m ⁻² .s ⁻²
$1/\tau$	log uniform on [1/24, 30] d ⁻¹

Appendix D: Model parameters

Appendix D.1: MCMC

To compute the uncertainties on the orbital elements, we perform a Monte Carlo markov chain analysis. In this appendix, we define the likelihood, priors, and convergence tests used.

We assume a Gaussian likelihood. Denoting by y the time series of radial velocities, the density y knowing the parameters is of the form

$$p(y|\theta, \eta) = \frac{1}{\sqrt{2\pi^N |V(\eta)|}} e^{\frac{1}{2}(y-f(\theta))^T V(\eta)^{-1} (y-f(\theta))}. \quad (\text{D.1})$$

Our signal model $f(\theta)$ includes a linear part, with an offset and the smoothed R'_{HK} as defined in appendix B.2. This one is centered and normalized by its standard deviation, so that its amplitude can be interpreted as a velocity, and Keplerian models initialised at 3.432, 5.198, 7.951, 12.03, 17.39 and 361 d. In total, θ is made of 32 parameters.

The noise model includes a free white noise jitter and an exponential decay term, so that the noise model is

$$V_{kl}(\eta) = \delta_{k,l}(\sigma_w^2 + \sigma_R^2) + \sigma_C^2 c(k, l) + \sigma_R^2 e^{-\frac{|t_k - t_l|}{\tau_R}} \quad (\text{D.2})$$

where $\eta = (\sigma_w, \sigma_R, \tau_R)$ are free parameters and σ_C is fixed to 1 m/s.

The prior distributions on the parameters are defined in table D.1. λ_0 is the mean longitude at the reference epoch 57500. The convergence is checked by computing the number of effective samples in each parameter chain as in Delisle et al. (2018). We find that each chain has at least 18,000 effective samples, which indicates convergence of the chain. To compute the uncertainties on the *msini* we assume a stellar mass of $1.08 \pm 0.1 M_\odot$.

Appendix D.2: Model consistency

It might happen that the parametrized model chosen (eq. D.1 and D.2) is such that even the maximum likelihood model does not account for the variations in the data. In that case, the orbital elements are not reliable as they are computed with an incorrect model.

To check whether the model is consistent with the data, we study the residuals. Following Hara et al. (2019b), we define

$$r_w := W(\hat{\eta})^{1/2} (y - f(\hat{\theta})) \quad (\text{D.3})$$

where y is the data, W is the inverse of the covariance matrix, f is the signal model and $\hat{\theta}, \hat{\eta}$ are the maximum likelihood values

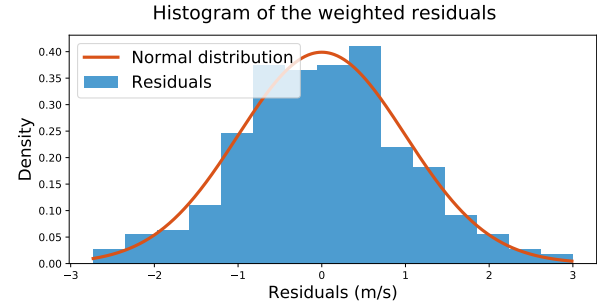


Fig. D.1. Histogram of the weighted residuals (blue) and probability density function of a normal variable (red).

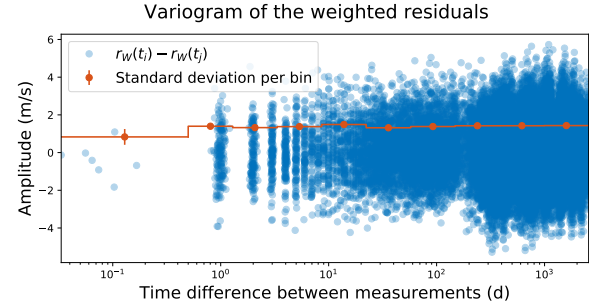


Fig. D.2. Difference between the weighted residuals as a function of the time interval between them (blue). The red stair curves represents the standard deviation of the residuals difference in each time bin.

of the parameters as given in table D.2. If the mode is consistent, then r_w should be approximately behaved as a Gaussian variable of mean 0 and variance 1.

In Fig. D.1, we represent the normalized histogram of r_w (blue) and the probability density function of a normal variable (red). We find that the behaviour of the residuals is consistent with a Gaussian density.

Secondly, we search for potential correlations in the weighted residuals. For all combinations of measurement times $t_i > t_j$ we represent $d_{ij} := r_w(t_j) - r_w(t_i)$ as a function of $t_j - t_i$. We then compute the standard deviation of the d_{ij} such that $t_j - t_i$ is in a certain time bin. Ten such intervals are considered, with a constant length in log scale. The results are represented in Fig. D.2, where it is apparent that there is no significant correlations remaining in the residuals. For comparison, in Fig. D.3 we show the same plots for the non weighted residuals of the model, where it appears that the dispersion of d_{ij} increase as a function of $t_j - t_i$.

In conclusion, there is no sign of missed variance and temporal correlations in the residuals, such that the signal model eq. D.1, D.2 seems appropriate.

Table D.2. Estimates and credible intervals of the orbital parameters for circular orbital models and a noise model including a jitter and a red noise model with exponential decay. We give three point estimates: the maximum likelihood, the posterior mean and median. The credible intervals are given as the shortest intervals containing $x\%$ of the sample with $x = 68.27, 95.45$ and 99.73% .

Parameter	ML fit	posterior mean	posterior median	68.27% confidence interval	95.45% confidence interval	99.73% confidence interval
offset	13537.200	13537.055	13537.065	[13536.50 , 13537.66]	[13535.87 , 13538.21]	[13535.18 , 13538.75]
smoothed rhk	-1.626	-1.490	-1.476	[-1.921 , -1.018]	[-2.421 , -0.591]	[-2.981 , -0.158]
Planet <i>b</i>						
P (d)	3.432037	3.432082	3.432081	[3.43182 , 3.43233]	[3.4315 , 3.4325]	[3.4312 , 3.4328]
K (m/s)	2.162	2.230	2.232	[2.01 , 2.44]	[1.80 , 2.65]	[1.58 , 2.85]
λ_0 (rad)	2.14786	2.12899	2.12896	[2.03 , 2.22]	[1.93 , 2.31]	[1.83 , 2.42]
$\sqrt{e} \cos \omega$	0.09461	-0.00582	-0.00521	[-0.13 , 0.14]	[-0.27 , 0.24]	[-0.38 , 0.35]
$\sqrt{e} \sin \omega$	0.05474	0.02084	0.01854	[-0.12 , 0.16]	[-0.24 , 0.29]	[-0.35 , 0.40]
$m \sin i$ (M_{\oplus})	5.80	5.52	5.51	[4.90 , 6.15]	[4.27 , 6.76]	[3.73 , 7.45]
Planet <i>c</i>						
P (d)	5.19884	5.19797	5.19797	[5.1970 , 5.1989]	[5.1960 , 5.1999]	[5.1949 , 5.2010]
K (m/s)	2.105	1.880	1.880	[1.64 , 2.12]	[1.39 , 2.36]	[1.14 , 2.60]
λ_0 (rad)	0.83406	0.84600	0.84559	[0.71 , 0.96]	[0.59 , 1.10]	[0.46 , 1.23]
$\sqrt{e} \cos \omega$	0.25572	0.08587	0.08267	[-0.07 , 0.24]	[-0.20 , 0.38]	[-0.30 , 0.50]
$\sqrt{e} \sin \omega$	-0.00946	-0.02288	-0.02228	[-0.17 , 0.12]	[-0.30 , 0.26]	[-0.42 , 0.36]
$m \sin i$ (M_{\oplus})	5.11	5.34	5.32	[4.57 , 6.09]	[3.85 , 6.88]	[3.15 , 7.67]
Planet <i>d</i>						
P (d)	7.95153	7.95122	7.95126	[7.9491 , 7.9534]	[7.9467 , 7.9556]	[7.944 , 7.958]
K (m/s)	1.889	1.793	1.793	[1.51 , 2.08]	[1.22 , 2.37]	[0.94 , 2.65]
λ_0 (rad)	0.51444	0.64356	0.64243	[0.48 , 0.79]	[0.33 , 0.95]	[0.16 , 1.14]
$\sqrt{e} \cos \omega$	-0.31161	-0.05532	-0.05165	[-0.19 , 0.11]	[-0.34 , 0.22]	[-0.46 , 0.33]
$\sqrt{e} \sin \omega$	0.28942	0.03202	0.03043	[-0.12 , 0.17]	[-0.24 , 0.32]	[-0.36 , 0.42]
$m \sin i$ (M_{\oplus})	6.82	5.87	5.85	[4.84 , 6.84]	[3.84 , 7.85]	[3.00 , 9.03]
Planet <i>e</i>						
P (d)	12.0322	12.0293	12.0293	[12.020 , 12.038]	[12.011 , 12.047]	[12.001 , 12.056]
K (m/s)	2.019	1.731	1.733	[1.40 , 2.07]	[1.05 , 2.40]	[0.69 , 2.74]
λ_0 (rad)	1.51355	1.55418	1.55301	[1.35 , 1.75]	[1.14 , 1.96]	[0.91 , 2.20]
$\sqrt{e} \cos \omega$	-0.28829	-0.00333	-0.00312	[-0.14 , 0.14]	[-0.30 , 0.27]	[-0.39 , 0.41]
$\sqrt{e} \sin \omega$	0.02799	3.51815	0.00071	[-0.15 , 0.14]	[-0.28 , 0.28]	[-0.40 , 0.41]
$m \sin i$ (M_{\oplus})	6.46	6.51	6.49	[5.15 , 7.78]	[3.87 , 9.19]	[2.545 , 10.65]
Candidate planet <i>f</i>						
P (d)	17.3924	17.4079	17.4052	[17.376 , 17.429]	[17.35 , 17.46]	[17.33 , 17.50]
K (m/s)	1.754	1.636	1.641	[1.26 , 2.02]	[0.86 , 2.40]	[0.44 , 2.80]
λ_0 (rad)	3.528	3.649	3.643	[3.38 , 3.89]	[3.13 , 4.17]	[2.81 , 4.55]
$\sqrt{e} \cos \omega$	-0.10	0.001	0.001	[-0.15 , 0.14]	[-0.29 , 0.29]	[-0.41 , 0.42]
$\sqrt{e} \sin \omega$	-0.23	-0.01	-0.01	[-0.16 , 0.14]	[-0.30 , 0.27]	[-0.44 , 0.40]
$m \sin i$ (M_{\oplus})	5.91	6.95	6.94	[5.24 , 8.58]	[3.592 , 10.42]	[1.76 , 12.3]
$m \sin i$ (M_{\oplus})	6.02	6.95	6.95	[5.21 , 8.56]	[3.681 , 10.45]	[1.61 , 12.1]
Yearly signal						
P (d)	374.32	370.70	370.06	[363.1 , 376.4]	[356.8 , 385.8]	[350.2 , 401.5]
K (m/s)	2.930	3.375	3.365	[2.63 , 4.09]	[1.90 , 4.88]	[1.12 , 5.78]
λ_0 (rad)	4.12470	3.64880	3.64428	[3.39 , 3.89]	[3.12 , 4.16]	[2.81 , 4.55]
$\sqrt{e} \cos \omega$	-0.05496	0.00134	0.00125	[-0.14 , 0.16]	[-0.29 , 0.29]	[-0.42 , 0.41]
$\sqrt{e} \sin \omega$	-0.09843	-0.01240	-0.01052	[-0.16 , 0.13]	[-0.30 , 0.28]	[-0.45 , 0.40]
Noise parameters						
σ_W (m/s)	1.990	1.208	1.242	[0.90 , 1.65]	[0.39 , 1.92]	[0.06 , 2.14]
σ_R (d)	9.851	3.246	3.246	[3.00 , 3.48]	[2.75 , 3.73]	[2.51 , 3.99]
τ (d)	3.947	5.265	4.893	[3.15 , 6.06]	[2.47 , 9.00]	[1.90 , 14.2]

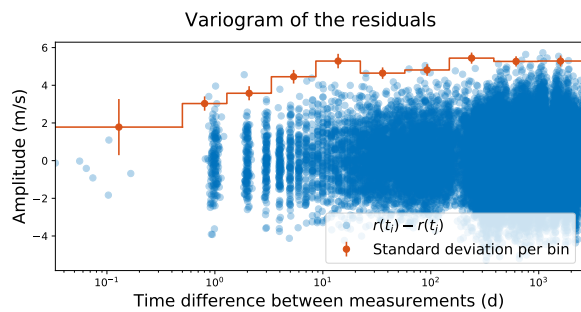


Fig. D.3. Difference between the residuals (not weighted) as a function of the time interval between them (blue). The red stair curves represents the standard deviation of the residuals difference in each time bin.